Adaptive optics for enhanced signal in CARS microscopy

A. J. Wright[1], S. P. Poland[1], J. M. Girkin[1*], C. W. Freudiger[2], C. L. Evans[2, 3], and X. S. Xie[2 *]

[1]*Institute of Photonics, SUPA, University of Strathclyde, 106 Rottenrow, Glasgow,G4 0NW, Scotland*
[2]*Department of Chemistry and Chemical Biology, Harvard University, 12 Oxford Street, Cambridge MA, 02138USA*
[3]*Current address: Wellman Center for Photomedicine, Massachusetts General Hospital, Harvard Medical School, Boston, MA 02114*
*Corresponding Authors: j.m.girkin@strath.ac.uk and xie@chemistry.harvard.edu

Abstract: We report the use of adaptive optics with coherent anti-Stokes Raman scattering (CARS) microscopy for label-free deep tissue imaging based on molecular vibrational spectroscopy. The setup employs a deformable membrane mirror and a random search optimization algorithm to improve signal intensity and image quality at large sample depths. We demonstrate the ability to correct for both system and sample-induced aberrations in test samples as well as in muscle tissue in order to enhance the CARS signal. The combined system and sample-induced aberration correction increased the signal by an average factor of ~3x for the test samples at a depth of 700 µm and ~6x for muscle tissue at a depth of 260 µm. The enhanced signal and higher penetration depth offered by adaptive optics will augment CARS microscopy as an *in vivo* and *in situ* biomedical imaging modality.

OCIS codes: (170.3880) Medical and biological imaging; (180.4315) Non linear microscopy; (220.1000) Aberration correction; (110.1080) Active or adaptive optics; (300.6230) Spectroscopy, coherent anti-Stokes Raman scattering.

References and Links

1. M. D. Cahalan, I. Parker, S. H. Wei, and M. J. Miller, "Real-time imaging of lymphocytes *in vivo*," Curr. Opin. Immunol. **15,** 372-377 (2003)
2. B. R. Masters and P. T. C. So, "Confocal microscopy and multi-photon excitation microscopy of human skin *in vivo*," Opt. Express **8,** 2-10 (2001).
3. G. Marques, L. Wang, S. P. Lin, S. L. Jacques, F. K. Tittel, S. L. Thomsen and J. Schwartz, "Measurement of Absorption and Scattering Spectra of Chicken Breast with Oblique Incidence Reflectometry," Proc. SPIE **2976,** 306-317 (1997)
4. M. Schwertner, M. J. Booth, and T. Wilson, "Characterizing specimen induced aberrations for high NA adaptive optics microscopy," Opt. Express **12,** 6540-6552 (2004).
5. F. Ganikhanov, S. Carrasco, X. S. Xie, M. Katz, W. Seitz, D. Kopf , "Broadly tunable dual-wavelength light source for coherent anti-Stokes Raman scattering microscopy," Opt. Lett., **31,** 1292-1294 (2006).
6. F. Helmchen and W. Denk, "Deep tissue two-photon microscopy," Nat. Methods **2,** 932-940 (2005).
7. W. R Zipfel, R. M. Williams, and W. W. Webb, "Nonlinear magic: multiphoton microscopy in the biosciences," Nat. Biotech. **21,** 1369 - 1377 (2003)
8. J. X. Cheng and X. S. Xie, "Coherent anti-Stokes Raman scattering microscopy: instrumentation, theory, and applications," J. Phys. Chem. B **108,** 827-840 (2004).
9. F. Ganikhanov, C. L. Evans, B. G. Saar, and X. S. Xie, "High sensitivity vibrational imaging with frequency modulation coherent anti-Stokes Raman scattering (FM-CARS) microscopy," Opt. Lett. **31,** 1872-1874 (2006).
10. C. L. Evans, E. O. Potma, M. Puoris'haag, D. Côté, C. P. Lin, and X. S. Xie, "Chemical imaging of tissue *in vivo* with video-rate coherent anti-Stokes Raman scattering microscopy," PNAS **102,** 16807-16812 (2005).
11. C. L. Evans, X. Xu, S. Kesari, X. S. Xie, S. T.C. Wong and G. S. Young, "Chemically-selective imaging of brain structures with CARS microscopy," Opt. Express **15,** 12076-12087 (2007)
12. J. X. Cheng, A. Volkmer, L. D. Book, X. S. Xie, "Multiplex Coherent Anti-Stokes Raman Scattering Microspectroscopy and Study of Lipid Vesicles," J. Phys. Chem. B **106**, 8493 (2002).
13. J. X. Cheng, S. Pautot, A. D. Weitz, and X. S. Xie, "Ordering of Water Molecules Between Phospholipid Bilayers Visualized by Coherent anti-Stokes Raman Scattering Microscopy," PNAS **100**, 9826-9830 (2003).

14. X. Nan, W. Y. Yan, and X. S. Xie, "CARS Microscopy: Lights Up Lipids in Living Cells," Bioph. Int. **11**, 44-47 (2004).
15. X. Nan, A. M. Tonary, A. Stolow, X. S. Xie, J. P. Pezacki, "Intracellular Imaging of HCV RNA and Cellular Lipids by Using Simultaneous Two-Photon Fluorescence and Coherent Anti-Stokes Raman Scattering Microscopies," ChemBioChem **7**, 1895-1897 (2006).
16. M. J. Booth, M. A. A. Neil, R. Juskaitis, and T. Wilson, "Adaptive aberration correction in a confocal microscope," PNAS **99**, 5788 (2002).
17. L. Sherman, J. Y. Ye, O. Albert, and T. B. Norris, "Adaptive correction of depth-induced aberrations in multiphoton scanning microscopy using a deformable mirror" J. Microscopy **206**, 65-71 (2002).
18. P. Marsh, D. Burns, and J. Girkin, "Practical implementation of adaptive optics in multiphoton microscopy," Opt. Express **11**, 1123-1130 (2003).
19. A. J. Wright, D. Burns, B. A. Patterson, S. P. Poland, G. J. Valentine, and J. M. Girkin, "Exploration of the Optimisation Algorithms used in the implementation of Adaptive Optics in Confocal and Multiphoton Microscopy," Microsc. Res. Tech. **67**, 36-44 (2005).
20. M. Rueckel, J. A. Mack-Bucher, and W. Denk, "Adaptive wavefront correction in two-photon microscopy using coherence-gated wavefront sensing," PNAS **103**, 17137 (2006).
21. R. K. Tyson, "Principles of adaptive optics," Principles of adaptive optics, Edition: 2nd ed., Publisher: Boston, MA: Academic Press, 1998, ISBN: 0127059024 (1998).
22. M. A. A. Neil, M. J. Booth, and T. Wilson, "Closed-loop aberration correction by use of a modal Zernike wave-front sensor," Opt. Lett. **25,** 1083-1085, (2000).
23. A. J. Wright, B. A. Patterson, S. P. Poland, J. M. Girkin, G. M. Gibson, and M. J. Padgett, "Dynamic closed-loop system for focus tracking using a spatial light modulator and a deformable membrane mirror," Opt. Express **14**, 222-228 (2005)
24. E. Dalimier and C. Dainty, "Comparative analysis of deformable mirrors for ocular adaptive optics," Opt. Express **13**, 4275-4285 (2005).
25. L. Zhu, P.-C. Sun, D.-U. Bartsch, W. R. Freeman, and Y. Fainman, "Wave-front generation of Zernike polynomial modes with a micromachined membrane deformable mirror," App. Opt. **38**, 6019-6026 (1999).
26. S. Tang, T. B. Krasieva, Z. Chen, and B. J. Tromberg, "Combined multiphoton microscopy and optical coherence tomography using a 12-fs broadband source," J. Biomed. Opt. **11,** 020502, (2006).
27. J. J. Dirckx, L. C. Kuypers, and W. F. Decraemer, "Refractive index of tissue measured with confocal microscopy," J. Biomed. Opt. **4** 044014 (2005).
28. E. J. Fernández and P. Artal, "Membrane deformation mirror for adaptive optics: performance limits in visual optics," Opt. Express **11**, 1056-1069 (2003).
29. A. J. Wright, S. P. Poland, J. Vijverberg, and J. M. Girkin, "A practical implementation of adaptive optics for aberration compensation in optical microscopy," Proc. 6th International Workshop on Adaptive Optics for Industry and Medicine, paper [30] (2007)

1. Introduction

Optical microscopy has proved to be an immensely powerful tool for biomedical applications, allowing for subcellular-level image resolution in living systems [1, 2]. A major problem in optical microscopy, however, is limited depth penetration compared to MRI and CT, because of light scattering [3], absorption and optical aberrations of the sample [4]. It is possible to improve penetration depth by utilizing longer excitation wavelengths in the near-IR region [5]. In this regime single-photon absorption and scattering cross-sections decrease while absorption, dominated by water, is still weak. A successful technique for deep tissue imaging using a near-IR excitation wavelength is two-photon fluorescence microscopy, which routinely images at depths of 500 μm and is capable of probing tissues at depths in excess of 1 mm [6]. Two-photon microscopy relies on the presence of fluorescent species that are either intrinsic to the tissue [7] or introduced as exogenous labels. However, there are situations for which fluorescent labeling is not desired. For example, small molecules often cannot be labeled without perturbing their functions and exogenous labeling is, in many cases, not possible for *in situ* imaging of patients.

Coherent anti-Stokes Raman scattering (CARS) microscopy provides chemically-selective image contrast based on the intrinsic vibrational modes of molecular species [8], avoiding the need for labels. CARS has greatly enhanced sensitivity compared to other vibrationally-selective modalities such as spontaneous Raman scattering [9], avoiding the long acquisition times typically encountered in vibrational imaging. CARS microscopy has been demonstrated to work at video-rate *in vivo* [10], enabling real-time imaging of living specimens. Most

CARS imaging systems [9-11] operate in the near-IR to maximize imaging depth and reduce multiphoton damage.

In CARS, two optical fields, called "pump" and "Stokes", with frequencies ω_p and ω_s respectively, are overlapped in time and space. When the beat frequency of the resulting field ω_p-ω_s matches the vibrational resonance of a molecular species, the molecular oscillators are driven resonantly. This coherent excitation leads to the generation of a strong, directional blue-shifted field at the anti-Stokes frequency $\omega_{as}=2\omega_p$-ω_s. The CARS intensity is given by $I_{as}=|\chi^{(3)}|^2 \cdot I_p^2 \cdot I_s$, where I_p and I_s are the intensities of the pump and the Stokes field respectively, and $\chi^{(3)}$ is the third-order nonlinear susceptibility. $\chi^{(3)}$ has vibrationally resonant and non-resonant components [12]. The later is independent of the Raman-shift and needs to be suppressed for high-sensitivity imaging [9]. Due to the non-linear nature of the CARS process, the signal is only generated at the focal spot, giving CARS microscopy inherent optical sectioning capabilities. The CARS signal is consistently strong, and does not experience the photobleaching effects that can limit fluorescence microscopy. CARS microscopy has been used to image distributions of DNA and protein [12], water [13], and lipids [14, 15] in living cells. Capabilities for biomedical imaging have been demonstrated *in vivo* in skin [10] and *ex vivo* in brain tissue [11]. In the later case it was possible to distinguish healthy brain tissue from tumorous tissue using intrinsic vibrational contrast, indicating clinical potential.

Like other optical imaging techniques, however, the imaging depth of CARS is also limited by sample turbidity. For example, the penetration depth in highly scattering brain tissue was limited to 80 µm in grey and 40 µm in white matter [11]. A technique to extend this penetration depth would be highly beneficial. In the last few years there has been considerable interest in using adaptive optics in optical sectioning microscopy, particularly confocal and two-photon microscopy, to improve image quality at depth [16-20].

Adaptive optics is a technique that has been used extensively in optical astronomy to overcome atmospheric aberrations that distort and degrade images of interstellar objects [21]. The key principle of adaptive optics is to shape the incoming optical wavefront in such a way to counteract such aberrations and restore image quality. The total aberrations present in optical microscopy arise from several contributions: imperfections in the optics and system misalignment (system-induced aberrations); mismatches in the refractive index between the immersion medium and the sample (depth-specific sample-induced aberrations); and local variations of the refractive index from the average due to the tissue structure (location-specific sample-induced aberrations).

The successful implementation of adaptive optics in optical sectioning microscopy is reliant on an accurate method for determining the aberration correction required. This has been achieved by measuring the aberrations introduced by the sample [20, 22], using an optimization algorithm technique that improves on a particular property of the image [19], or, actively locking to a specific aberration and tracking the correction required as the image depth increases [23].

Here we demonstrate the use of adaptive optics in CARS microscopy to overcome system and sample-induced aberrations. Using a deformable membrane mirror and a random search algorithm [19], we improve the CARS signal intensity in a 740 µm deep sample of agarose and polystyrene beads and a 260 µm thick sample of white chicken muscle tissue.

2. Methodology

2.1 CARS imaging system

The imaging system (Fig. 1) utilized an optical parametric oscillator (OPO) (Levante Emerald, APE-Berlin) synchronously pumped by a frequency doubled Nd:YVO$_4$ laser (picoTRAIN, High-*Q*, 7 ps, 532 nm, 76 MHz repetition rate). The OPO was based upon a temperature-tuned non-critically phase matched LBO (LiB$_3$O$_5$), providing collinear, temporally overlapped signal and idler output pulse trains [9]. A stacked Lyot filter, positioned at Brewster's angle in the cavity, provided fine wavelength tuning. The signal and

idler beams were used as the pump and Stokes beams, respectively, for the CARS process. For all experiments, the pump and Stokes wavelengths were set to 920 nm and 1254 nm to target the symmetric CH_2 stretching frequency.
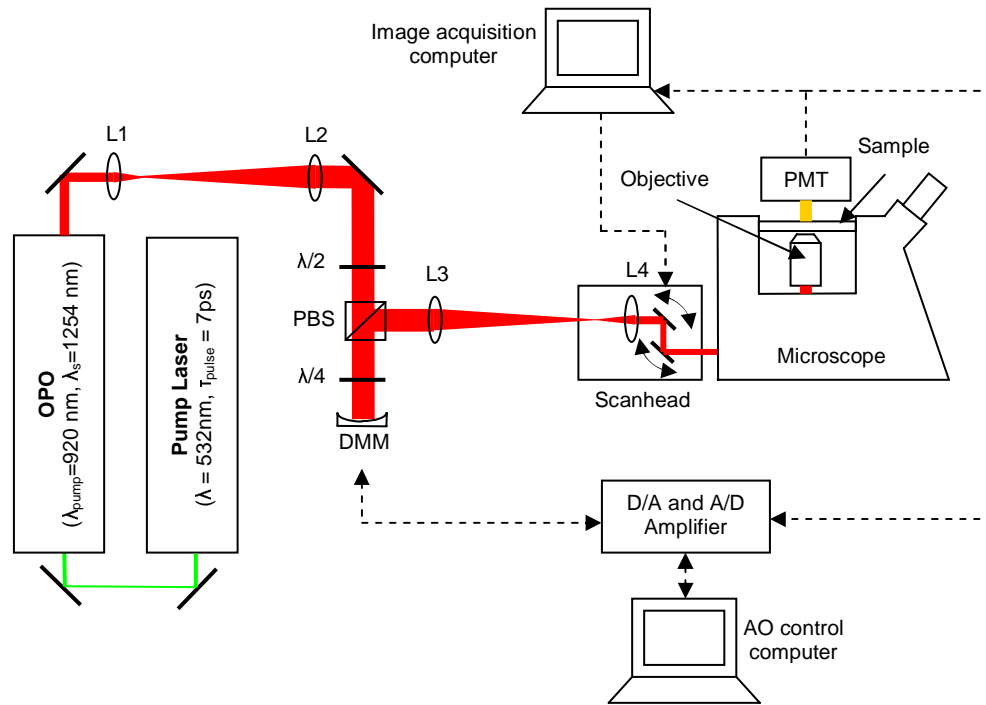

Fig. 1. Adaptive CARS setup. The signal and idler pulse trains exit the optical parametric oscillator (OPO) collinearly and overlapped in time. A set of achromatic lenses (L1, L2) expand and collimate the beam. The polarizing beam splitter cube (PBS) and quarter-waveplate form a double-pass configuration such that beams deflected by the deformable membrane mirror (DMM) are redirected to the microscope. A photomultiplier tube (PMT) collects the forward CARS signal.

The pump and Stokes beams were coupled into a modified inverted microscope (IX71/FV300, Olympus) optimized for near-IR throughput [11]. A 20X 0.75NA air objective (UPlanSApo UIS2, Olympus) with a working distance of ~0.6 mm (in air) was used for all imaging experiments. Due to low chromatic aberrations, this objective gives a very large CARS field of view, and is therefore ideal for tissue imaging. The CARS signal was always collected in the forward direction to keep imaging conditions similar between samples. All specimens were prepared with thicknesses less than 1 mm, and were sandwiched between No 1 coverslips, which are used routinely in CARS microscopy to provide increased working distance. The total power level at the microscope focus was kept at approximately 150 mW throughout the experiments. No photodamage effects were observed.

2.2 Adaptive optics system

A 15 mm diameter deformable membrane mirror (DMM) was used as the adaptive optic element to shape the incoming wavefront. The laser beams were initially expanded to approximately 10 mm in diameter with lenses L1 and L2. This is an accepted beam size for this particular DMM since the membrane is bound at the edges and by not completely filling the DMM we ensure that we only use the active region of the element [24, 25]. The DMM was integrated into the beamline in a perpendicular geometry, similar to that used previously

for confocal imaging [19], consisting of a polarizing beamsplitter cube and a λ/4-waveplate. A λ/2-waveplate was placed before the polarising beamsplitter cube, in order to ensure a correct initial polarization. The beams pass through a λ/4-waveplate in a double pass configuration that rotates the polarization by 90° after interaction with the DMM, resulting in the reflection of the outgoing beam by the polarizing beamsplitter cube. Lenses 3 and 4 were used to reduce the beam size to suit the scanning mirrors and to image the adaptive optic element onto the telecentric point, between the close-coupled scanners, which in turn was imaged onto the back aperture of the microscope objective.

The DMM consisted of 37 electrostatic actuators mounted below a silicon nitride membrane (Flexible Optical BV/OKO Tech, The Netherlands). The shape of the membrane was altered by applying a voltage of up to 175 V to the individual actuators. The maximum deformation of the DMM was measured to be ~7.5 μm using a Zygo interferometer. The DMM was controlled via a custom built electronics/software interface that used a random search optimization algorithm to determine a mirror shape for aberration compensation [19]. A figure of merit from the CARS image was fed into the optimization algorithm and the mirror shape was rapidly altered in order to optimize this value. Each step in the random search algorithm involved selecting an actuator at random, changing the voltage applied to that actuator by a random amount, then accepting or rejecting the change depending on if it led to an increase or a decrease in the figure of merit. The optimization algorithm was programmed to stop when it was unable to increase the figure of merit in the previous 2000 mirror changes. This optimization algorithm approach is well suited to CARS microscopy, since photobleaching does not occur and any signal enhancement from a fixed point in the samples leads directly to an enhancement in the resolution of the system, making signal intensity from a point in the image an ideal figure of merit. A control experiment verified that signal intensity increases were a result of aberration correction and not due to a beam size change at the objective back aperture that might alter the objective throughput.

The initial starting point for the DMM was set to correspond to the half way point for the maximum membrane deformation, and was equivalent to a adding a small quantity of defocus onto the incoming wavefront. The position of Lens L2 (Fig. 1) was adjusted slightly so that collimated light entered the microscope objective. This biased mirror setting allowed for the equivalent of both push and pull motions on the membrane so that both positive and negative aberration corrections could be made.

2.3 Sample preparation

The test sample consisted of scattering polystyrene beads embedded in agarose gel which has a refractive index of ~1.4 and is non transparent and scattering [26]. Samples were prepared from UltraPure[TM] Agarose (Invitrogen, USA) that was mixed and heated with TAE Buffer to 1% concentration. Approximately 0.01 ml of 10 μm diameter polystyrene beads in an aqueous suspension (Polyscience, Inc., USA) were mixed with 15 g of agarose gel in its liquefied heated state to achieve diluted bead concentrations ($\approx$ 100 beads per 500 μm stack of full field of view or ~2600 per mm^3). The agarose gel was sandwiched between two coverslips separated by a varying number of adhesive spacers (Grace Biolabs, USA), each with a thickness of 120 μm. The final thickness was measured on the microscope by taking a z-stack and correcting for the index of refraction of the gel numerically.

To demonstrate the capabilities of aberration corrected CARS images for deep tissue imaging, chicken breast muscle was used as a representative sample for tissue with low absorption and scattering properties [3]. The tissue naturally contained adipose deposits with a high concentration of fatty acids as well as distinguishable structures at all tissue depths. The fresh, unfrozen tissue was embedded in agarose gel and sliced using a vibratome (Ultracut, Leica Microsystems). All axial distances were adjusted to allow for the axial shift associated with focusing into a sample with a higher refractive index than the immersion media (in this case air) [27].

2.4 Image processing

An image of the background signal for the system was subtracted from all CARS images to solely display signal arising from resonant and non-resonant CARS. The main contributions of this background arose from the noise of the analog-to-digital converter (FV300, Olympus) and voltage offsets of the PMT pre-amplifier (Olympus). Image post-processing was accomplished using ImageJ with the UCSD Fluoview ImageJ Plugins and Igor Pro.

3. Results

3.1 System corrections

As a first step, we demonstrated the capability to correct for the system-induced aberrations by focusing the collinear pump and Stokes beams on the upper surface of a glass-air interface and detecting non-resonant CARS signal. As no sample is located between objective and focal spot, aberrations can only originate from the system itself. These aberrations are introduced from imperfect optics in the beam-path and the DMM, optical misalignment, as well as an incomplete correction of the microscope objective. Imaging a glass-air interface is a standard procedure to test the alignment of a CARS microscope. The exact position in z was chosen to maximize the CARS intensity in the center of the field of view. Ideally, the non-resonant CARS signal should be homogeneous through the field of view. Instead one sees a round spot at the center of the image (Fig. 2(a)) due to aberrations that vary across the scan and reduce the overlap of the pump and Stokes focal spots at large scan angles (beam walk-off). The DMM optimization algorithm was then used to maximize the non-resonant CARS intensity from the interface with the beams fixed at the image center.
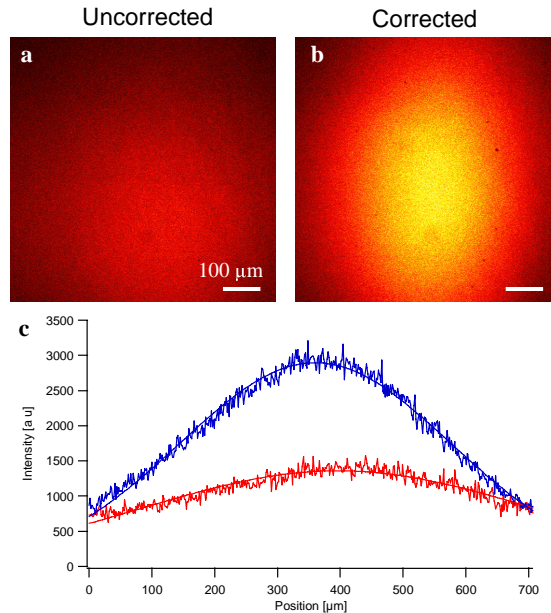

Fig. 2. Non-resonant CARS image obtained by raster-scanning of tightly focused collinear pump- and Stokes-beams with N.A. 0.75 air objective at an glass-air interface. a) Image without DMM correction. b) Image taken after optimizing DMM with a centered pump- and Stokes-beam. c) Horizontal cross-sections of a) and b) through the maximum, showing 2.2x CARS signal enhancement due to wavefront correction. Gaussian fits are added.

Figure 2(b) is the non-resonant CARS image taken by raster-scanning the collinear pump- and Stokes-beam while applying this optimized DMM setting. The image also shows a round spot whose cross-section is shown in Fig. 2(c) together with that of Fig. 2(a). A 2.2x signal

increase in the peak intensities in Fig. 2(b) compared to Fig. 2(a) was observed with a slight shift in the position of the center. The round spot still appears after correction as we could not correct for lateral-chromatic aberrations with a single DMM placed in the combined beam path.

3.2 Agarose/bead sample

To evaluate the aberration correction as a function of depth we used 1% agarose gel containing scattering polystyrene beads sandwiched between two coverslips as a controlled test sample. The Raman shift was tuned to 2845 cm^{-1} to excite a symmetric CH_2 stretch in the agarose and beads. The total CARS signal consists of these resonant contributions and the non-resonant background mainly form water. In addition to the system-induced aberrations corrected above, aberrations originating from the index of refraction mismatch between the coverslip and the sample and are expected to change as a function of the penetration depth. We maximized the CARS intensity by optimizing the DMM for centered pump and Stokes beams focused on the top glass-air interface for sample thickness of 0 μm (discussed above), 178 μm, 315 μm, 460 μm and 734 μm. In doing so we generated a look-up table (LUT) of optimized mirror shapes for these depths. Three dimensional image stacks of a 734 μm thick sample were obtained for each mirror-shape in the LUT as well as the uncorrected case.
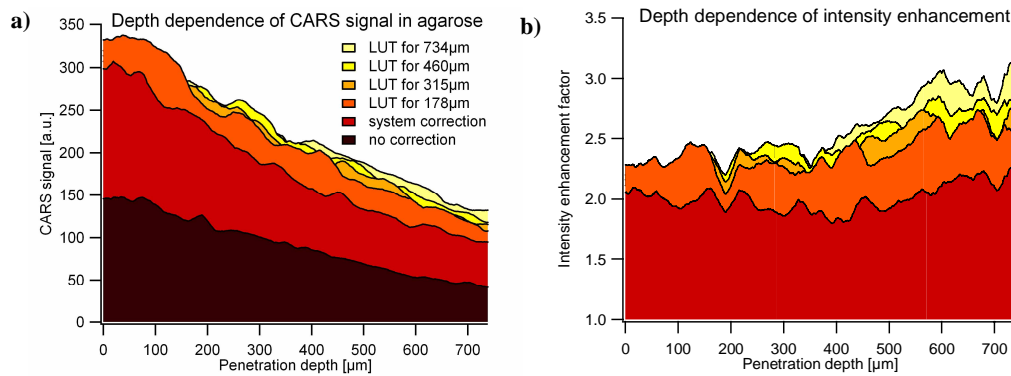

Fig. 3. Adaptive optics improvement of CARS intensity from a 734 µm thick agarose-bead sample. Graphs are smoothed at 25µm intervals to average laser intensity fluctuations that occurred while the xyz-stack was taken. a) Averaged CARS intensity as a function of depth using different look up tables. b) Enhancement factors (corrected intensity / uncorrected intensity) as a function of depth.

Figure 3(a) shows the average intensity of a 280 μm x 280 μm xy-image as a function of depth into the sample measured for each mirror-shape of the LUT. The system aberration correction was determined from a glass-air interface, as opposed to a glass-agarose interface, which led to a higher signal being achieved at 0 μm penetration depth using the 178 μm LUT rather than the system aberration correction LUT. Although the signal decreases as a function of the penetration depth for a given mirror-shape, signal enhancement at different depths is indeed achieved by DMM optimization. In fact, the optimized CARS signal at a depth of 734 μm was comparable to the CARS intensity normally obtained at the surface of the sample without any correction. Fig. 3(b) shows the depth-dependence of the signal enhancement factor, calculated by dividing the corrected signal intensity by the uncorrected signal intensity. As can been seen in Fig. 3(b), the larger the penetration depth, the greater the signal enhancement factor. Correction for system-induced aberrations alone produced a mean enhancement factor of 2.0, with a standard deviation of 0.14. For the different LUTs, there is no one mean enhancement factor for the entire depth stack due to the mirror shape being optimized for a particular depth. The relative error ($\Delta enh/enh$), where enh is the enhancement factor, is consistent for all LUT mirror shapes near zero depth (4%) and

increases for all mirror shapes by an addition 2% over the depth profile. The increase in standard deviation of these enhancement factors with depth is thought to be due to the accumulated optical aberrations caused by the agarose-bead sample heterogeneity. A maximum signal enhancement factor of 3.2x is obtained at the maximum working distance of the objective in agarose of 734 µm.

Figure 4 shows three CARS images of a polystyrene bead fixed in agarose gel taken at a depth of 592 µm into the sample without aberration correction, with only the system-induced aberrations corrected and with the system and sample-induced aberrations corrected with the LUT technique. The improvement in bead signal level demonstrates the enhancing effect of the adaptive optic approach. The image was taken at the Raman shift of CH_2 stretching with an image acquisition time of 5 ms per pixel for the 40x40 pixel section shown. The dark ring around the bead is due the index of refraction difference between polystyrene and agarose. Both resonant and nonresonant CARS signals arise due to the same combination of pump and Stokes beams. Therefore, the enhancement factors for beads distributed throughout the sample should match those of the agarose. Indeed, the enhancement factors for 22 randomly selected beads throughout the xyz stack correlate well with the enhancement factors shown in Fig. 3(b).
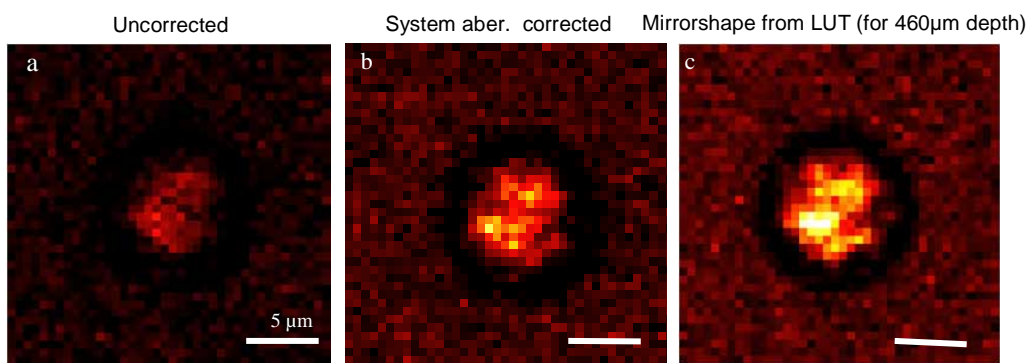

Fig. 4. CARS images of a polystyrene bead fixed in agarose gel at 592 µm depth in the sample a) without aberration correction b) with the system-induced aberration corrected using the DMM mirror-shape from the LUT for 0µm depth and c) with the system and sample-induced aberrations corrected using the LUT recorded at a depth of 460µm.

3.3 Tissue sample

To demonstrate deep tissue imaging we used a sample of adipose globular deposits in white chicken muscle. To target the fats present within the adipose cells, the CARS system was tuned to the CH_2 symmetric stretch of lipids (2845 cm^{-1}). These globular deposits were chosen as a suitable feature from which the CARS signal could be optimized due to the high concentration of fatty acids within adipose globular deposits, as well as their relatively high frequency throughout the tissue sample.

For a heterogeneous tissue sample, optimization was performed *in situ*, in order to correct for refractive index variations across the sample on region by region basis. Fig. 5 shows an image of a typical fat deposit at a depth of 260 µm in the tissue. The 3 images of the same structure, taken with the same imaging parameters, were obtained without aberration correction (Fig. 5(a)), with the system-induced aberration correction LUT (Fig. 5(b)) and with the *in situ* correction (Fig. 5(c)). The arrow shows the point at which the signal was optimized. The line-scans through the optimization points are shown beneath. We obtained a maximum enhancement factor of approximately 6x at the position of optimization.
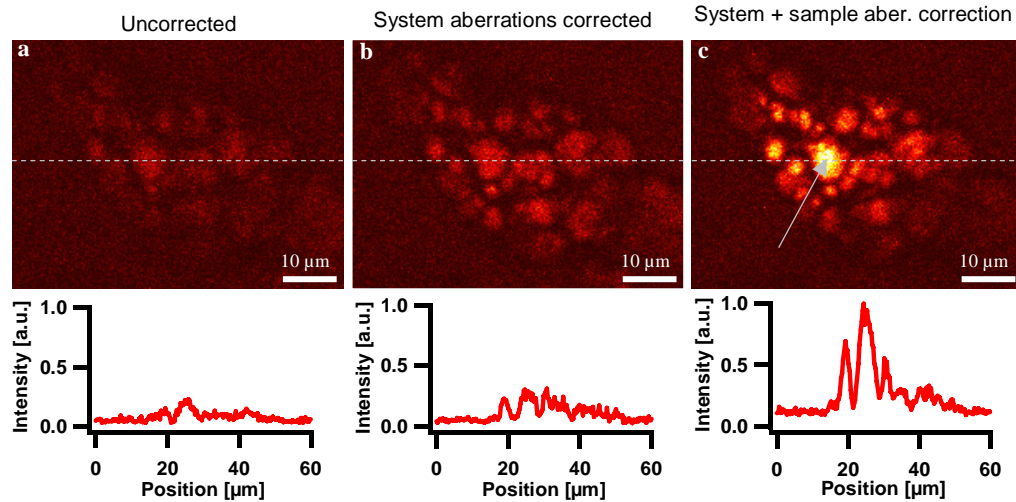
Fig. 5. Adipose globular deposit imaged with CARS microscopy at 260 µm depth in white chicken muscle. Top: Comparison of image a) without correction, b) with the system-induced aberrations corrected and c) with the system and sample-induced aberrations corrected for the globule marked by the arrow. Bottom: Horizontal linescans through the tip of the arrow, intensity-averaged over 3 adjacent lines.

The DMM shapes required to compensate for the system-induced and system and sample-induced aberrations can been seen in Fig. 6. By solving Poisson's partial differential equation the shape of the DMM was inferred from the applied actuator voltages and scaled with prior knowledge of the maximum deformation achievable [19, 28]. The DMM shape due to the bias position was calculated and adjusted for; hence, the images show positive and negative path difference corrections. By subtracting the system-induced correction from the system and sample-induced correction we are able to predict the DMM shape that would be required to correct for solely the sample-induced aberrations.
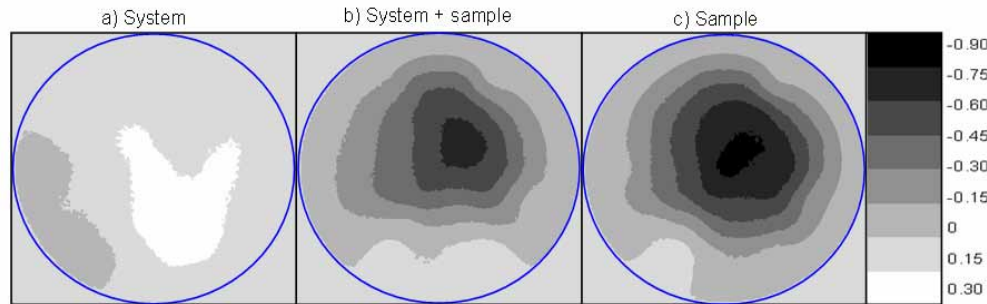

Fig. 6. DMM shapes required to compensate for a) the system aberrations, b) the system and sample aberrations and c) the sample only aberrations. The scale bar represents DMM deformation in microns and each image shows the 15mm diameter mirror.

Figure 7 shows the enhancement factor as a function of distance from the point of optimization. The decay of the enhancement factor with the distance from the point of optimization arises from the fact that the refraction index varies across the sample (blue line). In contrast, the signal taken with the system-induced aberration correction did not vary greatly (red line). At a position 20 µm from the point of optimization the *in situ* correction gave a greater enhancement factor than the system-induced aberration correction alone.
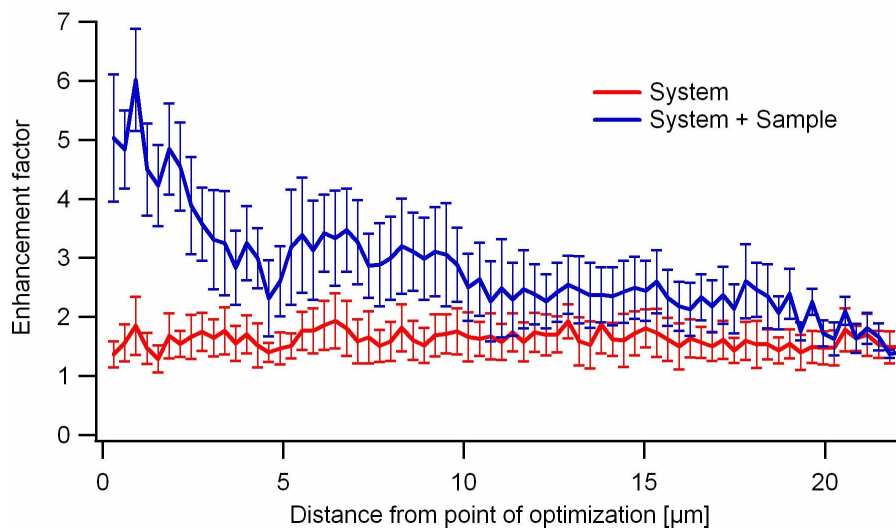
Fig. 7. Radial enhancement function displaying the average signal enhancement factor with standard deviations from adipose deposit at 260 µm depth as a function of the distance from the point of optimization (arrow in Fig. 5). The localized optimization on the deposit decays due to the heterogeneous distribution of the refraction index in tissue. The mirror-shape taken from the LUT for system-induced aberration correction gave an on average flat enhancement as it is not optimized for a particular position in the sample.

4. Discussion and conclusion

We have demonstrated aberration correction in a CARS microscope using an adaptive optic element. Maximum enhancement factors of approximately six times are of the same order as observed in comparable two-photon microscopy experiments [20]. Similar signal enhancement factors could be expected to be achieved when detecting back scattered signal, as is often required for *in vivo* imaging, since the backscattered signal originates from the forward scattered signal [10] and aberration correction would not affect the radiation pattern. This shows the promise of adaptive optics in overcoming penetration limits for deep tissue imaging with CARS microscopy. In addition, to greatly improving the signal intensity at depth, adaptive optics provides the user with the option to reduce the power of the two laser beams while still maintaining current levels of signal intensity.

In this work, we presented signal intensity improvements when using a look up table technique or when optimizing directly from a feature in the image. For future applications the choice of optimization method will be highly dependent on the sample being imaged and the information required. It is clear from Fig. 7 that optimizing directly on a feature produced an enhancement factor that varied across the image, peaking at the point of optimization, whereas, in contrast, the success of the LUT technique relies on applying a single correction to the whole field of view. When the depth-specific sample-induced aberrations dominate, such as when the sample is relatively homogenous as in the case of the agarose-bead sample, a LUT provides the ideal method for aberration correction. When taking an image in a heterogeneous sample, on the other hand, where the main focus of the image is a particular feature, it is more appropriate to optimize directly on that feature to remove depth-specific and location-specific sample-induced aberrations. In the case of the muscle tissue presented in section 3.3, applying the mirror-shape from the *in situ* optimization for the zoomed in field of view demonstrated that although the enhancement factor map was non-uniform there was still image improvement to be gained by using a single aberration correction [29].

In general, in order to maximize the enhancement factor and improve the convergence time of the algorithm an incremental approach was employed, where the initial DMM shape at the start of the optimization was either the system-induced aberration correction or a

correction obtained from a thinner sample. This effectively gave the algorithm an intelligent starting point and was found to be particularly useful when imaging deep into a sample where the initial signal-to-noise ratio was poor.

Another promising scenario for the application of adaptive optics is the mapping of the spatio-temporal dynamics of several regions of the sample. Often in imaging experiments, one is only interested in the behavior of select regions of the sample. For biomedical imaging it is feasible to scan the tissue with the system-induced aberrations corrected or by using a LUT from a material with similar optical properties to the tissue, until an interesting feature is found and an *in situ* optimization is performed. The best mirror shape from optimizing on this feature can then be established as a standard.

The optimization algorithm typically converged after 3000 mirror shapes and the algorithm currently stops when the fitness parameter has not improved significantly in the previous 2000 mirror changes. In addition, the mirror was not run at full speed, resulting in optimization times of approximately 3-4 minutes. Adjusting the convergence parameter and running the mirror at the maximum update rate of 1kHz will result in significantly reduced optimization times in the future.

When correcting for system-induced aberrations, it was seen that applying an aberration correction resulted in a slightly shifted image field of view. In this case, such a shift had the positive effect of centering the field of view and correcting for minor microscope misalignments. If necessary, this shift could be limited by choosing an alternative figure of merit, such as the average intensity of the image, or, by grouping the search space into Zernike modes and removing tip and tilt [20]. The addition of the adaptive optics system in the standard CARS setup is likely to contribute to the system-induced aberrations, although from previous experience, and the technique of initially aligning the system with a plain mirror rather than the DMM, we believe aberrations arising from imperfections in the DMM were minimal.

With a simple optical arrangement, involving a single DMM placed pre-scanning in the combined pump and Stokes beam paths, we have demonstrated the potential for adaptive optics in CARS imaging. This approach holds promise for future *in vivo* and *in situ* CARS microscopy applications.

Acknowledgements